



# Morphology effect of Ru/CeO<sub>2</sub> catalysts for the catalytic combustion of chlorobenzene



Hao Huang, Qiguang Dai, Xingyi Wang\*

Laboratory for Advanced Materials, Research Institute of Industrial Catalysis, East China University of Science and Technology, Shanghai 200237, PR China

## ARTICLE INFO

### Article history:

Received 7 November 2013

Received in revised form

27 December 2013

Accepted 29 January 2014

Available online 6 February 2014

### Keywords:

Ceria

Ruthenium

Chlorobenzene

Catalytic combustion

Crystal plane dependence

## ABSTRACT

The present work elucidated the morphology and crystal-plane effects of nanoscale ceria on the activity of Ru/CeO<sub>2</sub> catalysts toward catalytic combustion of chlorobenzene taken as a model of chlorinated aromatic hydrocarbons (CAHs). CeO<sub>2</sub> nanorods (CeO<sub>2</sub>-r), nanocubes (CeO<sub>2</sub>-c) and nano-octahedra (CeO<sub>2</sub>-o) (enclosed by {110} and {100}, {100} and {111}, respectively) as supports, were prepared by wet impregnation. The status and structure of Ru species is quite dependent on the enclosed various facets. Ru/CeO<sub>2</sub>-r possesses much more Ru<sup>4+</sup>, oxygen vacancies and Ru–O–Ce bonds than Ru/CeO<sub>2</sub>-c and Ru/CeO<sub>2</sub>-o, indicating that there is a stronger interaction between Ru and CeO<sub>2</sub>-r. The surface oxygen mobility and reducibility follow the order of Ru/CeO<sub>2</sub>-r > Ru/CeO<sub>2</sub>-c > Ru/CeO<sub>2</sub>-o. The activity test of chlorobenzene oxidation shows that Ru/CeO<sub>2</sub>-r is more active than that of Ru/CeO<sub>2</sub>-c and Ru/CeO<sub>2</sub>-o, with T<sub>10%</sub> and T<sub>90%</sub> of 160 and 280 °C, respectively, which can be related to a larger number of Ru–O–Ce bonds, higher content of Ru<sup>4+</sup> and surface oxygen mobility and reducibility. These results confirm that the activity of Ru/CeO<sub>2</sub> catalysts for CB oxidation is greatly affected by CeO<sub>2</sub> shape/crystal plane.

© 2014 Published by Elsevier B.V.

## 1. Introduction

CAHs continue to attract considerable public concern because of their persistence in the environment, bioaccumulation in the tissues and potential toxicity as carcinogens and teratogens [1]. CAHs are released together with other unintentionally persistent organic pollutants (UPOPs) from thermal process like incinerators and metal industries [2]. Therefore, it is important to develop convenient, practical and cost effective methods to remove atmospheric CAHs. Among various available techniques, catalytic combustion has been proven to be a promising and emerging technology for the removal of CAHs in waste gases, due to its highly effective character (between 250 and 550 °C) and low use of energy (without additional fuel) when compared to a thermal process [3].

Of the studies of the catalysts used in the catalytic combustion of CAHs, most have been reported on the three types of catalysts based on noble metals [4–6], transition metals [7–11] and zeolites [5,12]. Among all these catalysts, ceria-based catalyst has attracted much attention due to its remarkable redox properties and oxygen storage capability (OSC). In our previous works [13–17], one kind of ceria-based catalyst, i.e. MnO<sub>2</sub>–CeO<sub>2</sub> catalyst was found to be a very active catalyst for CAHs catalytic combustion. However, it is notable that most studies on ceria-based catalysts were carried on ceria nanoparticles of polycrystal. Numerous

theoretical simulations have indicated that different crystal planes of ceria would drastically affect the catalytic property and performance, such as surface stability [18,19], oxygen vacancies formation energy [20,21], and interaction with surface molecules [22] and metals like Pt [23] and Pd [24]. Through the morphology control of the CeO<sub>2</sub> particle, the concept of morphology-dependent nanocatalysis not only enables the fundamental understanding of the structure-reactivity relationship, but also highlights essential implications for the design and preparation of more efficient CeO<sub>2</sub> and CeO<sub>2</sub>-based catalysts. Therefore, recent studies in CeO<sub>2</sub> systems have focused on the structure and crystal/shape-dependent properties. For example, Li et al. have obtained single-crystalline CeO<sub>2</sub> nanorods ({110} and {100}) for CO oxidation, and have found that CeO<sub>2</sub> nanorods are more reactive than other counterparts [25]. Yan et al and Xing et al. have synthesized single-crystalline CeO<sub>2</sub> nanocubes ({100}) and CeO<sub>2</sub> nano-octahedra ({111}) by hydrothermal treatment respectively [26,27]. Overbury et al. have studied CeO<sub>2</sub> nano-crystals with well-defined surface planes for CO oxidation and the activity follows rods > cubes > octahedra, which can be ascribed to different mobility of lattice oxygen [28]. Dai et al. have investigated catalytic oxidation of DCE and EA over ceria exposed well-defined crystal planes, and CeO<sub>2</sub> nanorods turned out to be more preferable than the other two, for its higher OSC and higher mobility of oxygen [29]. Murciano has studied ceria with different morphology for oxidation of naphthalene. It was found that nanorods were more reactive than the other two, giving higher oxygen storage capacity and consequently a higher oxidation catalytic activity [30]. Moreover, the shape of CeO<sub>2</sub> nanoparticles has

\* Corresponding author. Tel.: +86 21 64253372; fax: +86 21 64253372.

E-mail address: [wangxy@ecust.edu.cn](mailto:wangxy@ecust.edu.cn) (X. Wang).

also been reported to strongly affect the metal–CeO<sub>2</sub> interaction and thus tuned up the catalytic performance of CeO<sub>2</sub>-supported metal catalysts like Au [31], Ag [32] and Cu [33].

Our recent studies on the combustion of chlorobenzene (CB) showed that Ru/CeO<sub>2</sub> catalyst possesses highly stable activity for a long time [34]. The reaction mechanism involved in that C–Cl bond in CB could be dissociated easily on Ce<sup>3+</sup>/Ce<sup>4+</sup> active sites and the dissociated CB could be rapidly oxidized into CO<sub>2</sub> and H<sub>2</sub>O by surface reactive oxygen or lattice oxygen. The chlorine species adsorbed on the active sites could be removed in the form of Cl<sub>2</sub> via the Deacon reaction catalyzed by RuO<sub>2</sub> or CeO<sub>2</sub> [35]. However, there is no available information about Ru/CeO<sub>2</sub> catalyst in the literature related to the shape/crystal plane effect of nanoscale CeO<sub>2</sub> on the chemical state, structure and the reactivity of Ru species. Therefore, for better understanding of the metal-support interactions between Ru and CeO<sub>2</sub>, the correlation of the activity of Ru/CeO<sub>2</sub> catalyst for CB oxidation with the shape and crystal plane of nanoscale ceria was investigated.

In this paper, we employed CeO<sub>2</sub>-*r*, CeO<sub>2</sub>-*c* and CeO<sub>2</sub>-*o* as supports to prepare Ru/CeO<sub>2</sub> catalysts. The concentration and structure of oxygen vacancies and Ru–O–Ce in Ru/CeO<sub>2</sub> catalysts were investigated by means of microstrain and Raman spectroscopy, and correlated with the Ru–CeO<sub>2</sub> interaction. Combining with X-ray diffraction (XRD), high-resolution transmission electron microscopy (HRTEM), diffuse reflectance UV-vis spectroscopy, X-ray photoelectron spectroscopy (XPS), hydrogen temperature-programmed reduction (H<sub>2</sub>-TPR) and oxygen temperature-programmed desorption (O<sub>2</sub>-TPD), we found that the shape-dependent of Ru/CeO<sub>2</sub> catalyst for CB oxidation were related to different status of Ru, oxygen mobility caused by oxygen vacancies, Ru–O–Ce bond and redox ability.

## 2. Experimental

### 2.1. Catalysts preparation

#### 2.1.1. Preparation of CeO<sub>2</sub> with well-defined facets

CeO<sub>2</sub>-*r*, CeO<sub>2</sub>-*c* and CeO<sub>2</sub>-*o* were prepared by a hydrothermal process as described in Refs. [25–27]. To obtain CeO<sub>2</sub>-*r* and CeO<sub>2</sub>-*c*, 3 g of Ce(NO<sub>3</sub>)<sub>3</sub>·6H<sub>2</sub>O and 35.4 g (9.2 g for CeO<sub>2</sub>-*c*) of NaOH were dissolved in 80 mL of deionized water, respectively. Then, these two solutions were mixed and kept stirring for 30 min with the formation of milky slurry. Subsequently, the mixed solution was transferred into a Teflon-lined stainless steel autoclave and then heated at 100 and 180 °C for 48 and 24 h to get CeO<sub>2</sub>-*r* and CeO<sub>2</sub>-*c*, respectively. After hydrothermal treatment, the precipitates were washed with distilled water and ethanol, then dried at 60 °C for 12 h and calcined in air (increasing from room temperature to 350 °C at the rate of 1 °C/min and then maintaining at 350 °C for 3 h). For CeO<sub>2</sub>-*o*, 0.87 g of Ce(NO<sub>3</sub>)<sub>3</sub>·6H<sub>2</sub>O and 0.0076 g of Na<sub>3</sub>PO<sub>4</sub> were dissolved in 80 mL of distilled water. After being stirred at room temperature for 0.5 h, the mixed solution was transferred into a Teflon-lined stainless steel autoclave and heated at 170 °C for 10 h. After being cooled to room temperature, the precipitates were washed with distilled water and ethanol, then dried at 60 °C for 12 h and calcined in air (increasing from room temperature to 350 °C at the rate of 1 °C/min and then maintaining at 350 °C for 3 h).

#### 2.1.2. Preparation of Ru/CeO<sub>2</sub>

All three Ru/CeO<sub>2</sub> catalysts were prepared using the wet impregnation method. Typically, 0.5 g CeO<sub>2</sub> nanocrystal was slurried in deionized water under stirring, and the desired amount of 0.198 M (0.02 g<sub>Ru</sub> mL<sup>-1</sup>) RuCl<sub>3</sub> aqueous solution was added dropwise. After the impregnation, the sample was dried in a vacuum oven at RT

and then calcined in air at 400 °C for 4 h (increases from room temperature to 400 °C at the rate of 1 °C min<sup>-1</sup> and maintains for 4 h at 400 °C). The loading of Ru was calculated of 0.4% (weight ratio) for Ru/CeO<sub>2</sub> catalysts.

### 2.2. Catalysts characterization

The powder XRD of samples were recorded on a Rigaku D/Max-rC powder diffractometer using Cu K $\alpha$  radiation (40 kV and 100 mA). The microstrain ( $\varepsilon$ ) of these samples were determined from line-broadening measurements on the different crystal planes, using the equation  $\varepsilon = \beta/4tg\theta$ . The nitrogen adsorption and desorption isotherms were measured at 77 K on an ASAP 2400 system in static measurement mode. The specific surface area was calculated using the Brunauer–Emmett–Teller (BET) model. Ruthenium content was determined by X-ray fluorescence (XRF) using a Shimadzu (XRF-1800) wavelength dispersive X-ray fluorescence spectrometer. The Raman spectra were obtained on a Renishaw in Viat + Reflex spectrometer equipped with a CCD detector at ambient temperature and moisture-free conditions. The emission line at 514.5 nm from an Ar<sup>+</sup> ion laser (Spectra Physics) was focused, analyzing spot about 1 mm, on the sample under the microscope. The power of the incident beam on the sample was 3 mW. Time of acquisition was varied according to the intensity of the Raman scattering. The wave numbers obtained from spectra were accurate to within 2 cm<sup>-1</sup>. UV-Vis diffuse reflectance spectra (DRS) were recorded in the range of 200–900 nm by using a Varian Cary-500 spectrophotometer. XPS measurements were made on a VG ESCALAB MK II spectrometer by using Mg K $\alpha$  (1253.6 eV) radiation as the excitation source. HRTEM images were taken on a JEM-2100F field emission transmission electron microscope that operated at 200 kV. Scanning electron microscope (SEM) images were recorded on a Hitachi-S4800 equipped with FEG (cold) in SE mode.

H<sub>2</sub>-TPR of samples placed at the bottom of the U-shaped quartz tube was investigated. Prior to the H<sub>2</sub>-TPR test, the sample (100 mg) was pre-treated with Ar flow (30 mL/min) at 400 °C for 3 h. The test was performed by heating the samples (100 mg) in H<sub>2</sub> (5 vol.%)/Ar flow (30 mL/min) at a heating rate of 10 °C/min from 50 to 600 °C. The hydrogen consumption was monitored by thermocconductivity detector (TCD), and the extent of reduction was quantitatively calculated according to the TPR peak areas and the result was calibrated on the basis of the hydrogen consumption from the reduction of CuO to Cu. O<sub>2</sub>-TPD was carried out in a U-shaped quartz tube and the desorption signal of oxygen was recorded with an online mass spectrometer apparatus (HIDEN QIC-20). Prior to O<sub>2</sub>-TPD test, the sample (100 mg) was pre-treated in a purified oxygen stream at 400 °C for 60 min, cooled down to room temperature in oxygen atmosphere and purged by a stream of purified He until stabilization of MS base line. The reactor was heated at the rate of 10 °C/min from 50 to 700 °C. Simultaneously, the desorbed oxygen signal was collected by MS detector.

### 2.3. Catalytic activity measurements

Catalytic combustion reactions were carried out in a continuous flow micro-reactor constituted of a quartz tube of 4 mm of inner diameter at atmospheric pressure. 200 mg catalyst as the reaction bed was packed. The feed flow through the reactor was set at 100 cm<sup>3</sup> min<sup>-1</sup> and the gas hourly space velocity (GHSV) was maintained at 30,000 h<sup>-1</sup>. Feed stream to the reactor was prepared by delivering liquid CB with a syringe pump into dry air and the injection point was electrically heated to ensure complete evaporation of the liquid reaction feeds. The concentration of CB in the reaction feeds was set at 1000 ppm. The temperature of the reactor was measured with a thermocouple located just at the bottom of the micro-reactor and the effluent gases were analyzed by an

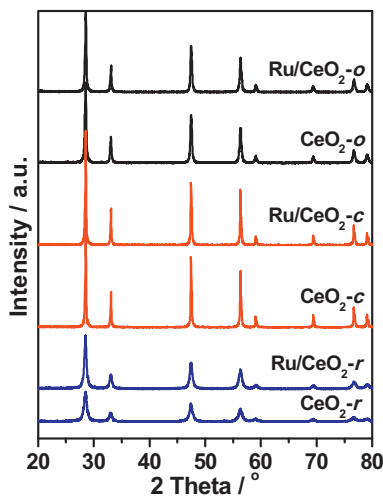


**Fig. 1.** XRD patterns of various  $\text{CeO}_2$  and  $\text{Ru}/\text{CeO}_2$  catalysts with well-defined facets.

on-line gas chromatograph equipped with a flame ionization detector (FID). Catalytic activity was measured over the range 100–400 °C and conversion data were calculated by the difference between inlet and outlet concentrations. Conversion measurements and product profiles were taken after maintained for 5 min at each test temperature and the conversion datum on the given temperature is the average value of five sampling analyses.

The concentrations of  $\text{Cl}_2$  were analyzed by the effluent stream bubbling through a 0.0125 M NaOH solution, and chlorine concentration was then determined by the titration with ferrous ammonium sulphate (FAS) using N, N-diethyl-p-phenylenediamine (DPD) as indicator [36]. Here, it should be noted that the total error caused in these processes may be within ±5%. The concentration of chloride ions in the bubbled solution was determined by using a chloride ion selective electrode [37].

### 3. Results and discussion

#### 3.1. Structural and morphological analysis

**Fig. 1** shows XRD patterns of  $\text{CeO}_2$  and  $\text{Ru}/\text{CeO}_2$  samples. All the peaks of  $\text{CeO}_2$ -r,  $\text{CeO}_2$ -c and  $\text{CeO}_2$ -o samples can be indexed to the face-centered cubic fluorite structure with space group Fm-3m (JCPDS 34-0394). Mean crystallite size, as calculated by Scherrer equation, is 11.9 nm for the  $\text{CeO}_2$ -r, 43.4 nm for the  $\text{CeO}_2$ -c, and 31.7 nm for the  $\text{CeO}_2$ -o (Table 1). After the introduction of Ru species, there appears no any new diffraction peak corresponding to  $\text{RuO}_2$  phase (at around 28° or 35°) or Ru phase (at around 44°). The absence of peaks related to Ru species may be attributed to a low content of Ru impregnated over the ceria, the entrance of Ru species into the ceria lattice, and high dispersion of Ru species of a small diameter size. The Bragg angle of cerianite shifting to slightly high value indicates that maybe some  $\text{Ru}^{4+}$  species ( $r_{\text{Ru}}^{4+} = 0.62 \text{ \AA}$ ) enters the fluorite-like lattice ( $r_{\text{Ce}}^{4+} = 0.94 \text{ \AA}$ ), leading to the decrease in the lattice parameters (Table 1) and the formation of Ru–O–Ce structure to some extent [34]. Moreover, the sinter caused by subsequent calcinations after the impregnation with aqueous  $\text{RuCl}_3$  solution results in a slight increase in the particle size (Table 1). In addition, the microstrain in  $\text{CeO}_2$  lattice (kinks, steps, dislocations, vacancies, etc.), which is mainly caused by oxygen defects [38,39], is estimated based on XRD data. Table 1 shows that  $\text{CeO}_2$ -r has much higher lattice strain both before and after Ru impregnation than  $\text{CeO}_2$ -c and  $\text{CeO}_2$ -o. It can be deduced that the density of oxygen defects in  $\text{Ru}/\text{CeO}_2$ -r may be much larger than that in the  $\text{Ru}/\text{CeO}_2$ -c and  $\text{Ru}/\text{CeO}_2$ -o. Moreover, the addition of ruthenium species led to a

decrease in the strain of the supports, suggesting that there was a strong interaction between Ru and  $\text{CeO}_2$ -r.

SEM and TEM observations were performed on all the samples in order to fully characterize their shapes and surface states. As shown in Fig. 2(a),  $\text{CeO}_2$ -r nanoparticles exhibit a narrow diameter distribution of  $12 \pm 2 \text{ nm}$  but a wide length distribution between 80 and 200 nm, selectively exposing {100} and {110} crystal planes [Fig. 2(b)].  $\text{CeO}_2$ -c nanoparticles are uniform with their edge lengths mostly between 33 and 43 nm [Fig. 2(c)] and expose {100} crystal planes [Fig. 2(d)]. SEM micrographs of  $\text{CeO}_2$ -o are dominated by a truncated octahedral shape enclosed by {111} facets with very uniform in size distribution (70–80 nm) [Fig. 2(e) and (f)]. Calculated average size of  $\text{CeO}_2$ -o is much larger than the sizes calculated based on XRD data, probably due to the fact that smaller particles broaden XRD peaks. The selected area electron diffraction (SAED) confirms that  $\text{CeO}_2$ -r,  $\text{CeO}_2$ -c and  $\text{CeO}_2$ -o are of single-crystalline nature [insert of Fig. 2(b), (d) and (f)].

Fig. 3 shows TEM and HRTEM photos of  $\text{Ru}/\text{CeO}_2$  samples. With the incorporation of Ru species, no evident change of the morphology is observed for these three nanoshapes. The loading of ruthenium was determined by X-ray fluorescence to be 0.38–0.42 wt% (Table 1), close to the expected value for each sample. Although the low metal loading of the catalysts prevented to obtain the metal particle size distributions, since not many  $\text{RuO}_2$  particles were visible from the HRTEM data, we could still find some Ru/RuO<sub>2</sub> nanoparticles attached on the specific shape-controlled surface of ceria.  $\text{RuO}_2$  on  $\text{Ru}/\text{CeO}_2$ -r,  $\text{Ru}/\text{CeO}_2$ -c and  $\text{Ru}/\text{CeO}_2$ -o exists in the form of ellipsoidal nanoparticles, as evidenced by their lattice fringe of 0.317 nm, corresponding to  $\text{RuO}_2$  {110} [Fig. 3(c), (f), (h)] [40,41]. Meanwhile spherical Ru nanoparticles can be identified with their lattice fringe of 0.205 nm, corresponding to Ru {101} [Fig. 3(e), (f), (i)] [40]. The average size of observed Ru or  $\text{RuO}_2$  nanoparticles in  $\text{Ru}/\text{CeO}_2$ -r and  $\text{Ru}/\text{CeO}_2$ -c is 6–8 nm, while for  $\text{Ru}/\text{CeO}_2$ -o, the average size of these particles is about 10 nm.

It should be noted that the size of  $\text{CeO}_2$ -o or  $\text{Ru}/\text{CeO}_2$ -o obtained by TEM is larger than that calculated by XRD results. In this work, the  $\text{CeO}_2$ -o and  $\text{Ru}/\text{CeO}_2$ -o samples were analyzed by XRD and TEM several times. And the results were repeated. As a result, there is not a good correlation between the crystal size of the  $\text{CeO}_2$ -o and  $\text{Ru}/\text{CeO}_2$ -o samples calculated by XRD and TEM. In our previous work [29], this difference between XRD and HRTEM for  $\text{CeO}_2$ -o was also reported. Possible cause is that only larger particles can be seen by TEM probably due to the shelter of smaller particles by larger ones.

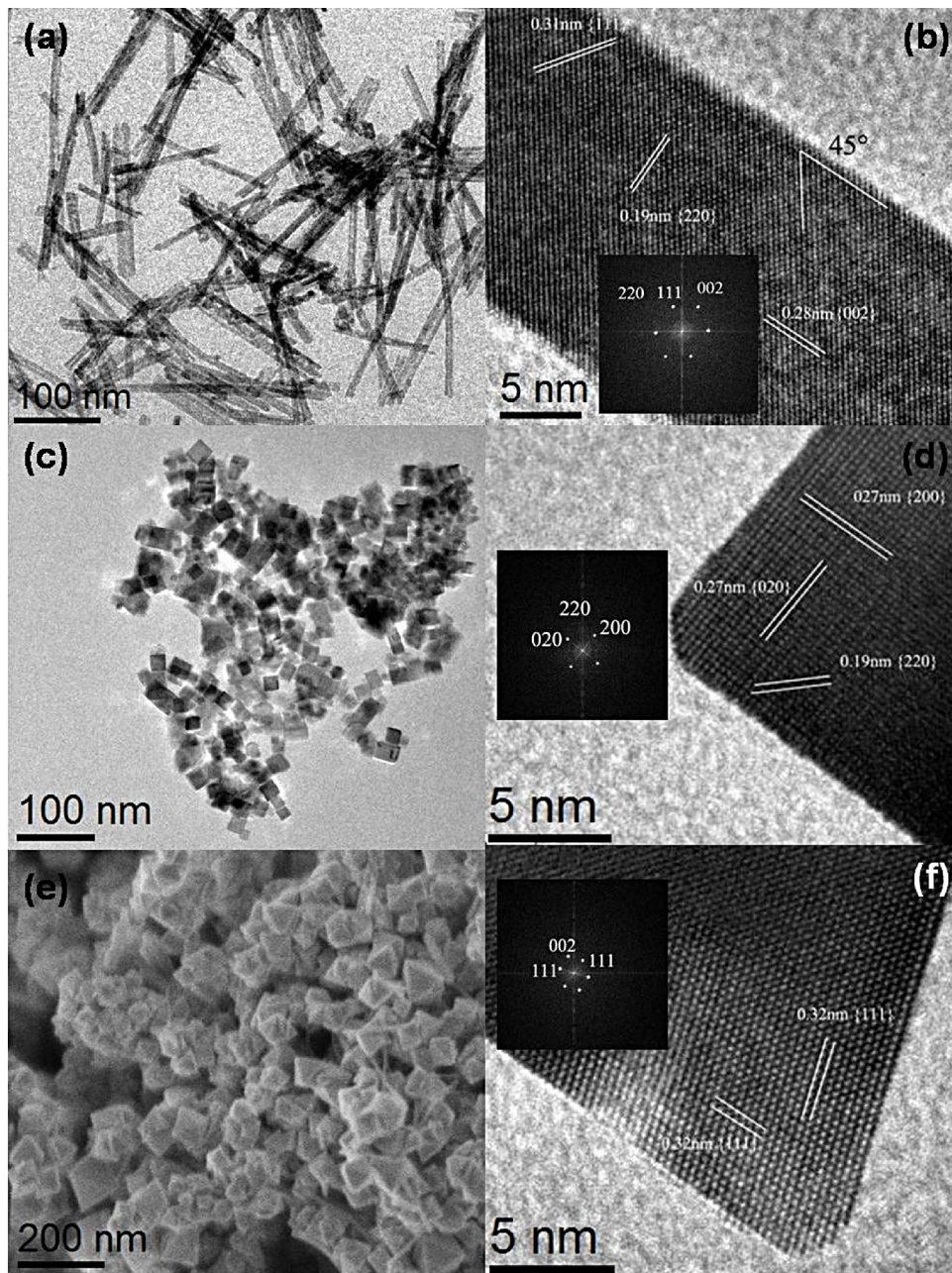
Thermogravimetric and Differential Thermal Analysis profiles of the  $\text{Ru}/\text{CeO}_2$  catalysts are presented in Fig. S1. All three samples show nearly no weight loss even up to 800 °C indicating a good purity, negligible adsorbed water and no loss of Ru species. Catalysts were also characterized using nitrogen adsorption–desorption. As a result, the isotherms for all catalysts are similar, confirming that the porosity results from inter-particle spaces and cannot be destroyed by the addition of Ru (Fig. S2). The BET areas of  $\text{Ru}/\text{CeO}_2$ -r,  $\text{Ru}/\text{CeO}_2$ -c and  $\text{Ru}/\text{CeO}_2$ -o are 58, 21, and  $18 \text{ m}^2/\text{g}$ , respectively. Furthermore, the pore volume of  $\text{CeO}_2$ -o sample significantly decreases after the introduction of Ru, indicating that Ru species have possibly been incorporated into the stacking pores of  $\text{CeO}_2$ -o (Table S1).

Fig. 4 shows Raman spectra of  $\text{CeO}_2$  and  $\text{Ru}/\text{CeO}_2$  samples. The Raman spectra of  $\text{CeO}_2$  are dominated by a strong  $F_{2g}$  mode of fluorite phase at  $460 \text{ cm}^{-1}$  with weak bands at 258, 597, and  $1172 \text{ cm}^{-1}$ , due to second-order transverse acoustic (2TA) mode, defect-induced (D) mode, and second-order longitudinal optical (2LO) mode, respectively [29]. As reported, for pure  $\text{RuO}_2$ , the bands at 528, 644, and  $716 \text{ cm}^{-1}$ , assignable to  $E_g$ ,  $A_{1g}$ , and  $B_{2g}$  modes, will appear [42]. However, since the intensities of these bands are very low compared to that of the bands assignable to  $\text{CeO}_2$ , these bands

**Table 1**

Structure and physical parameters of various samples.

Sample	Ru loading <sup>a</sup> (wt%)	S <sub>BET</sub> <sup>b</sup> (m <sup>2</sup> g <sup>-1</sup> )	Particle size <sup>c</sup> (nm)	Mean size <sup>d</sup> (nm)	Lattice parameters (nm)	ε(%)		
						(111)	(200)	(220)
CeO <sub>2</sub> -r	-	56	(12±2)×(80–200)	11.9	0.5416	1.16	1.11	0.78
CeO <sub>2</sub> -c	-	22	38±5	38.3	0.5413	0.32	0.28	0.20
CeO <sub>2</sub> -o	-	18	75±5	31.7	0.5412	0.44	0.38	0.27
Ru/CeO <sub>2</sub> -r	0.38	58	(11±3)×(50–200)	14.7	0.5413	0.94	0.86	0.62
Ru/CeO <sub>2</sub> -c	0.42	21	30±15	39.2	0.5412	0.33	0.29	0.20
Ru/CeO <sub>2</sub> -o	0.40	18	65±5	33.1	0.5408	0.41	0.37	0.27

<sup>a</sup> Determined by XRF.<sup>b</sup> Surface area determined from N<sub>2</sub> isotherm.<sup>c</sup> Calculated for about 100 nanoparticles from the TEM images.<sup>d</sup> Estimated by the Scherrer equation, applied to the (111) reflection of fluorite CeO<sub>2</sub>.**Fig. 2.** TEM, HRTEM and SAED (insert) images of CeO<sub>2</sub>-r (a and b) and CeO<sub>2</sub>-c (c and d); SEM, HRTEM and SAED (insert) images of CeO<sub>2</sub>-o (e and f).

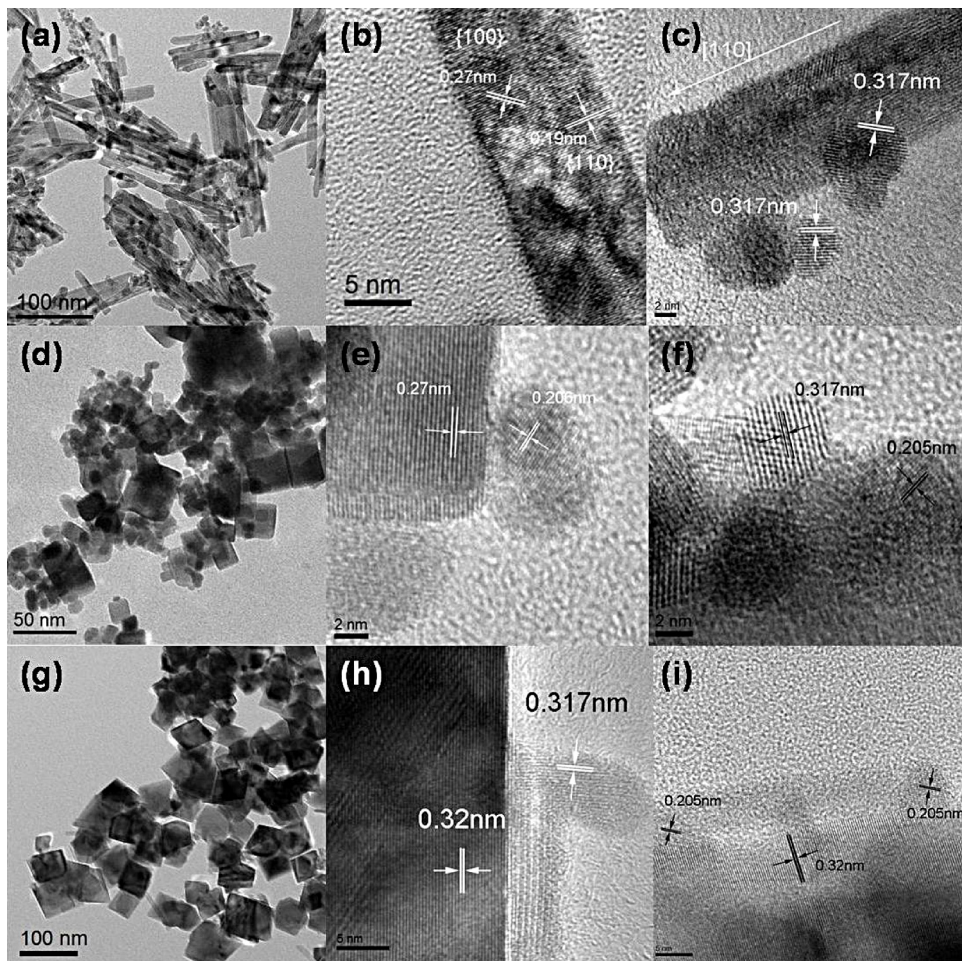


**Fig. 3.** TEM and HRTEM images of Ru/CeO<sub>2</sub>-r (a, b and c), Ru/CeO<sub>2</sub>-c (d, e and f) and Ru/CeO<sub>2</sub>-o (g, h and i).

are not detectable in the spectra of the Ru/CeO<sub>2</sub> samples, probably due either to their small amount or to the interaction between Ru species and ceria (consistent with XRD results). Only two new bands appear at 695 and 974 cm<sup>-1</sup>, as observed by Satsuma et al. [43]. The new bands cannot be attributed to other ruthenium oxides having various oxidation states (800 cm<sup>-1</sup> for RuO<sub>3</sub>, 822–881 cm<sup>-1</sup> for RuO<sub>4</sub>, 808 cm<sup>-1</sup> for RuO<sub>4</sub><sup>2-</sup>, 380–440 and 590 cm<sup>-1</sup> for hydrated RuO<sub>2</sub>) [44–46], and therefore, probably result from the interaction between Ru and CeO<sub>2</sub> (especially CeO<sub>2</sub> in highly oxidized state). Lin et al. found the interaction between Pt and CeO<sub>2</sub> by Raman spectroscopy and included the formation of Pt–O–Ce bond [47]. Here, it is reasonable for us to tentatively assign these new bands to Ru–O–Ce bond.

We performed the peak fitting of F<sub>2g</sub>, defect-induced modes and asymmetric structure of Ru–O–Ce in the Raman spectra of various samples. The ratios of I<sub>(1172+600)/I<sub>460</sub></sub>, which reflect the intrinsic defect concentration such as oxygen vacancy [33], are summarized in Table 2. The ratio for CeO<sub>2</sub>-r is significantly higher than those for the other two nanoceria samples, suggesting that CeO<sub>2</sub>-r have the most abundant oxygen vacancy sites. Theoretical calculation studies show that the vacancies formation energy on different crystal planes of CeO<sub>2</sub> follows the order of {110} < {100} < {111} [20]. This phenomenon is also consistent with other results reported in the literature [29,48]. After the loading of Ru, the ratios of I<sub>(1172+600)/I<sub>460</sub></sub> increases notably, for example, from 0.09 to 0.17 for Ru/CeO<sub>2</sub>-r, from 0.04 to 0.07 for Ru/CeO<sub>2</sub>-c and from 0.02 to 0.06 for Ru/CeO<sub>2</sub>-o. DFT study indicated that the Ru dopant activates lattice oxygen by the creation of longer Ce–O and Ru–O bond lengths compared

to those in CeO<sub>2</sub> and RuO<sub>2</sub> metal oxides [49], and thus facilitates oxygen vacancy through acting as the seed for the formation of oxygen vacancy clusters on the ceria surfaces. Moreover, in order to investigate the shape-dependent of surface Ru–O–Ce structure concentration, we calculated the ratios of I<sub>(695+974)/I<sub>460</sub></sub> through peak fitting, and listed them in Table 2. Clearly, Ru/CeO<sub>2</sub>-r presents much higher value of I<sub>(695+974)/I<sub>460</sub></sub> than the other two Ru/CeO<sub>2</sub> samples. It is noted that the bands at 695 and 974 cm<sup>-1</sup> for Ru/CeO<sub>2</sub>-o is almost not observed. Thus, the strength of interaction between Ru species and CeO<sub>2</sub> nanocrystals exposing the specific crystal planes follows as {110} > {100} » {111}.

### 3.2. Chemical states and reduction behavior of catalysts

UV-Vis DRS in Fig. 5 show that CeO<sub>2</sub>-r, CeO<sub>2</sub>-c and CeO<sub>2</sub>-o exhibit two intense absorption bands with maximum at about 276 and

**Table 2**  
Raman spectrum data and H<sub>2</sub> consumption.

Sample	Raman spectra		H <sub>2</sub> consumption (μmol g <sup>-1</sup> )	
	I <sub>(1172+600)/I<sub>460</sub></sub>	I <sub>(695+974)/I<sub>460</sub></sub>	LT	HT
CeO <sub>2</sub> -r	0.09	-	-	519
CeO <sub>2</sub> -c	0.04	-	-	250
CeO <sub>2</sub> -o	0.02	-	-	318
Ru/CeO <sub>2</sub> -r	0.17	0.080	1032	146
Ru/CeO <sub>2</sub> -c	0.07	0.025	596	58
Ru/CeO <sub>2</sub> -o	0.06	0.006	358	330

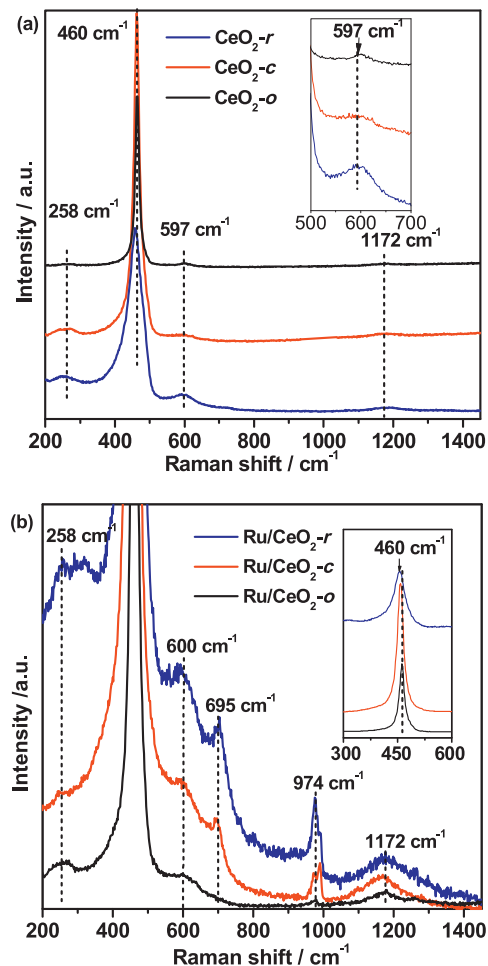


Fig. 4. Raman spectra of various CeO<sub>2</sub> (a) and Ru/CeO<sub>2</sub> (b) catalysts.

342 nm. According to previous literature report [50], the bands can be ascribed to the overlapping of the O<sup>2-</sup> → Ce<sup>4+</sup> charge transfer and interband transitions, respectively. The introduction of Ru species greatly enhanced the absorbance of CeO<sub>2</sub> in the visible light region. These experimental results well explain the colors of Ru/CeO<sub>2</sub> samples (Fig. S3). Meanwhile, a clearly visible peak could be observed in the visible light region of Ru/CeO<sub>2</sub>-r, Ru/CeO<sub>2</sub>-c and Ru/CeO<sub>2</sub>-o, centering at 480, 470, and 687 nm, respectively. This feature can be reasonably assigned to the surface plasmon resonance (SPR) peak of Ru nanoparticles supported on CeO<sub>2</sub>. The SPR peak red-shifts of Ru or RuO<sub>2</sub> nanoparticles increase with

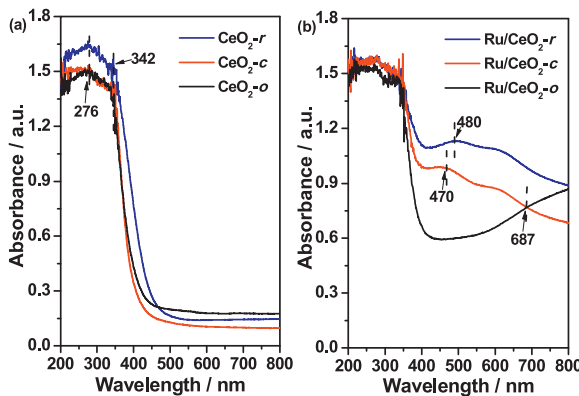


Fig. 5. UV-Vis spectra of various CeO<sub>2</sub> (a) and Ru/CeO<sub>2</sub> (b) catalysts.

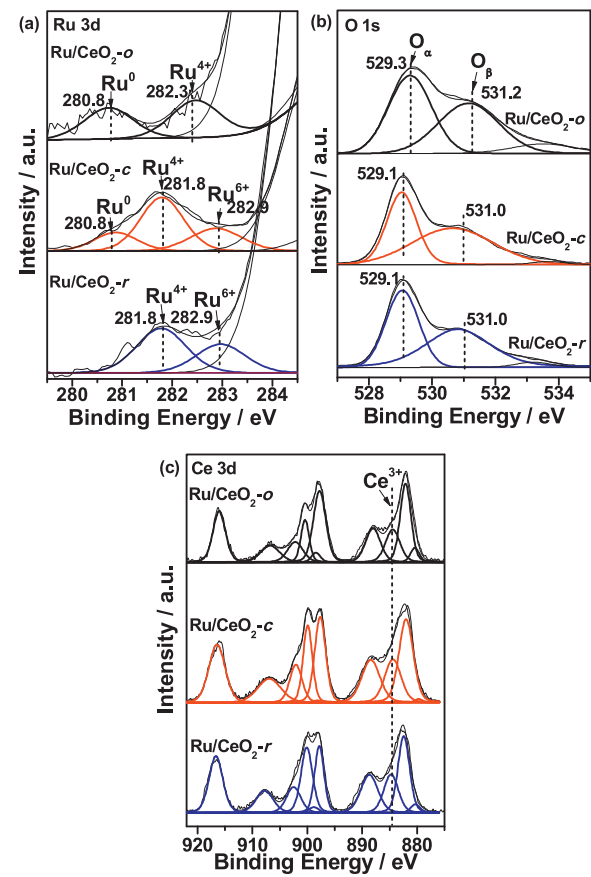


Fig. 6. XPS spectra of Ru 3d (a), O 1s (b), Ce 3d (c) for different Ru/CeO<sub>2</sub> catalysts.

the increase in their particle size [51,52]. Therefore, the average size of Ru or RuO<sub>2</sub> nanoparticles follows the order as Ru/CeO<sub>2</sub>-r ≈ Ru/CeO<sub>2</sub>-c < Ru/CeO<sub>2</sub>-o, which is consistent with the size order of Ru/CeO<sub>2</sub> nanoparticle obtained by HRTEM analyses. Moreover, the band at 480 nm for Ru/CeO<sub>2</sub>-r samples is much stronger than that for Ru/CeO<sub>2</sub>-c and Ru/CeO<sub>2</sub>-o. It is well known that the difference in the peak intensity generally depends on ion density and the chemical environment. Therefore, these results indicate that the morphology and crystal planes of nanoscale ceria resulted in different coordination environments of the supported Ru or RuO<sub>2</sub>.

Fig. 6 presents XPS spectra of Ru 3d, Ce 3d and O 1s for Ru/CeO<sub>2</sub> samples. The chemical states of Ru species on the surface of catalysts are obviously shape-dependent. As shown in Fig. 6(a), Ru/CeO<sub>2</sub>-r exhibits two Ru 3d<sub>5/2</sub> peaks at 281.8 and 282.9 eV that could be assigned to Ru<sup>4+</sup> and Ru<sup>6+</sup>, respectively [34,53]; Ru/CeO<sub>2</sub>-c exhibits one more Ru 3d<sub>5/2</sub> peak at 280.8 eV that could be assigned to Ru<sup>0</sup>; Ru/CeO<sub>2</sub>-o exhibits two Ru 3d<sub>5/2</sub> peaks at 280.8 and 282.3 eV that could be assigned to Ru<sup>0</sup> and Ru<sup>4+</sup>, respectively. Therefore, positively charged Ru species dominates in Ru/CeO<sub>2</sub>-r, whereas metallic Ru nanoparticles present in Ru/CeO<sub>2</sub>-c and Ru/CeO<sub>2</sub>-o. Moreover, the content of Ru<sup>4+</sup> follows: Ru/CeO<sub>2</sub>-r > Ru/CeO<sub>2</sub>-c > Ru/CeO<sub>2</sub>-o (Table 3). Ru<sup>4+</sup> ions possess a preference for insertion into the surface lattice of CeO<sub>2</sub>, which can induce the increase of oxygen vacancies concentration in the nanostructure CeO<sub>2</sub>. The results of composition analyses based on XPS data are listed in Table 3. Ru/CeO<sub>2</sub>-r presents a middle level of Ru/(Ru + Ce) ratio, while Ru/CeO<sub>2</sub>-c, the highest value. Combining the analyses with HRTEM, low Ru/(Ru + Ce) ratio in Ru/CeO<sub>2</sub>-r is normally attributed to probable insertion of Ru species into the surface layer of CeO<sub>2</sub> structure and incorporation of Ru species inside

**Table 3**  
XPS data of various samples.

Sample	Composition (at.%)					Ru/(Ru + Ce) (at.)	Ru <sup>4+</sup> (at.%)	$O_\beta/O_\alpha$	Ce <sup>3+</sup> (at.%)
	Ru	Ce	O	C	Cl				
Ru/CeO <sub>2</sub> -r	0.32	19.7	46.3	33.7	0.0	0.016	60.8	1.12	20.6
Ru/CeO <sub>2</sub> -c	0.60	19.5	45.4	34.3	0.1	0.029	54.1	1.06	19.1
Ru/CeO <sub>2</sub> -o	0.10	19.7	45.0	35.2	0.0	0.005	53.0	0.93	18.9

the pores, which can possibly confine the aggregation of RuO<sub>2</sub> particles. For Ru/CeO<sub>2</sub>-c, a higher surface composition could be due to a lower available surface area. Moreover, the fact that a much lower Ru/(Ru + Ce) ratio in Ru/CeO<sub>2</sub>-o was observed shows a possibility of the incorporation of Ru<sup>4+</sup> into the bulk of CeO<sub>2</sub> lattice [34].

The O1s spectra for Ru/CeO<sub>2</sub> catalysts clearly show that three states of surface oxygen exist [Fig. 6(b)]. The binding energy of 529.1–529.3 eV, denoted as O<sub>α</sub>, is characteristic of lattice oxygen. The peak at 531.0–531.2 eV is assigned to oxide defects or surface oxygen ions (O<sub>β</sub>) with low coordination, while the peak at 533 eV, to other possible oxygen species, such as surface carbonate or hydroxyl species [54]. The O<sub>β</sub>/O<sub>α</sub> ratio estimated through deconvolution method shows that the content of surface oxygen species on CeO<sub>2</sub> nanoparticles is of dependence on shape/crystal plane (Table 3). Ru/CeO<sub>2</sub>-r has the highest O<sub>β</sub>/O<sub>α</sub> ratio, probably due to its best incorporating with Ru<sup>4+</sup> which results in the most oxygen defect concentration on the surface. This effect has also been reported for the introduction of a range of other ions into the CeO<sub>2</sub> lattice [55].

Fig. 6(c) presents Ce 3d spectra. Ten peaks resulting from the pairs of spin orbit doublets can be identified through deconvolution method, of which six peaks at 882.4, 888.7, 897.6, 900.1, 907.7 and 916.6 eV arise from Ce<sup>4+</sup> contributions and four peaks at 880.2, 884.6, 898.7 and 902.6 eV, from Ce<sup>3+</sup> contributions [56]. The amount of Ce<sup>3+</sup> is estimated to be 20.6, 19.1 and 18.9% for Ru/CeO<sub>2</sub>-r, Ru/CeO<sub>2</sub>-c and Ru/CeO<sub>2</sub>-o, respectively. Therefore, Ce species exist mainly in Ce<sup>4+</sup> oxidation state in all three samples. Ce<sup>3+</sup> induces the formation of oxygen vacancies in the material, which are essential for absorption/dissociation of oxygen molecules during the oxidation reaction. Here, combining with UV-Vis DRS and XPS results, it can be concluded that the chemical states of Ru/CeO<sub>2</sub> samples are obviously affected by the crystal plane of CeO<sub>2</sub>, while Ru/CeO<sub>2</sub>-r with {110} and {100} plane has higher proportion of Ru<sup>4+</sup>, surface oxygen and smaller particle sizes of RuO<sub>2</sub>.

### 3.3. Redox properties of the catalysts

H<sub>2</sub>-TPR measurement was used to investigate the reducibility of surface oxygen in each catalyst (Fig. 7). The reduction of ceria surface oxygen occurs with the maxima at 520, 530 and 585 °C for CeO<sub>2</sub>-r, CeO<sub>2</sub>-c and CeO<sub>2</sub>-o, respectively, while the order of H<sub>2</sub> consumption is CeO<sub>2</sub>-r (519 μmol g<sup>-1</sup>)>CeO<sub>2</sub>-o (318 μmol g<sup>-1</sup>)>CeO<sub>2</sub>-c (250 μmol g<sup>-1</sup>) (Table 2), indicating that the reduction of ceria surface oxygen can be influenced significantly by the morphology. The fact that CeO<sub>2</sub>-r presents the highest reducibility could be associated with its high oxygen mobility and high specific surface area [26]. With the incorporation of Ru into CeO<sub>2</sub>-r and CeO<sub>2</sub>-c, there appear three reduction peaks. The surface reduction starts at 64 °C with maximum at 90 °C, which could be attributed to the reduction of adsorbed oxygen and Ru species. The corresponding H<sub>2</sub> consumptions are estimated to be 198 μmol g<sup>-1</sup>. The second peaks at 144 °C can be related to the Ru species incorporated into the surface of ceria and the surface oxygen of CeO<sub>2</sub> around Ru species. At this reduction step, H<sub>2</sub> consumption of Ru/CeO<sub>2</sub>-r is 834 μmol g<sup>-1</sup>, much higher than that of Ru/CeO<sub>2</sub>-c (398 μmol g<sup>-1</sup>). H<sub>2</sub> consumptions on the basis of RuO<sub>2</sub>+2H<sub>2</sub>→Ru<sup>0</sup>+2H<sub>2</sub>O should be 99 μmol g<sup>-1</sup>. It is reasonable

to deduce that so high H<sub>2</sub> consumption of Ru/CeO<sub>2</sub>-r should be resulted from the reduction of a large amount of surface oxygen of CeO<sub>2</sub>-r that is really promoted by the existence of Ru-O-Ce. The third peak is ascribed to the reduction of the surface oxygen of CeO<sub>2</sub> far away from Ru species. Compared with the reduction temperature of pure CeO<sub>2</sub>-r and CeO<sub>2</sub>-c, a significant decrease in the reduction temperature is due to relaxing Ce-O bond strongly bounded with Ru species, the same as observed in the case of Au/CeO<sub>2</sub>-r [31]. For Ru/CeO<sub>2</sub>-o, the reduction of Ru species starts at 171 °C with maximum at 216 °C and is overlapped by the reduction of Ru-O-Ce in the surface layer. The reduction of surface oxygen of CeO<sub>2</sub> and Ru-O-Ce in the bulk structure occurs at 276 °C. These results are in accordance with XRD, Raman and XPS data, which confirms that the relaxing Ce-O bond has a strong interaction with Ru species, leading to the formation of Ru-O-Ce structure. Obviously, the formation of Ru-O-Ce is greatly influenced by the shape/crystal plane of ceria. Ru/CeO<sub>2</sub>-r ({110} and {100}) and Ru/CeO<sub>2</sub>-c ({100}) with more structure of Ru-O-Ce are preferred surfaces for anchoring and dispersing Ru. Meantime, their surface oxygen can be reduced more easily than that of Ru/CeO<sub>2</sub>-o ({111}).

O<sub>2</sub>-TPD is an effective method to determine the mobility of oxygen species. As shown in Fig. 8, for CeO<sub>2</sub> supports, only CeO<sub>2</sub>-r displays one oxygen peak centered at 170 °C, which can be attributed to the physically adsorbed oxygen, while CeO<sub>2</sub>-c and CeO<sub>2</sub>-o give no oxygen peak below 500 °C, which can be expected based on bulk thermodynamics [57]. However, after the introduction of Ru, a distinctive feature is observed: Ru/CeO<sub>2</sub>-r gives three obvious oxygen desorption peaks at 180, 306 and 424 °C, while Ru/CeO<sub>2</sub>-c and Ru/CeO<sub>2</sub>-o only give two oxygen desorption peaks (105/368 and 170/347 °C). Generally, the adsorbed oxygen changes in the following procedures: O<sub>2</sub> (ad)→O<sub>2</sub><sup>-</sup> (ad)→O<sup>-</sup> (ad)→O<sup>2-</sup> (lattice) [58]. The physically adsorbed oxygen O<sub>2</sub> (ad) and chemically adsorbed oxygen O<sub>2</sub><sup>-</sup>/O<sup>-</sup> (ad) species are much easier to desorb than the lattice O<sup>2-</sup> species [59]. Therefore, at very low temperature (<200 °C), the desorption can be assigned to the physically adsorbed oxygen and/or the ordinarily chemically adsorbed oxygen, while the desorption peaks between 200 and 500 °C can be related to the chemically adsorbed oxygen species (CAOS) on

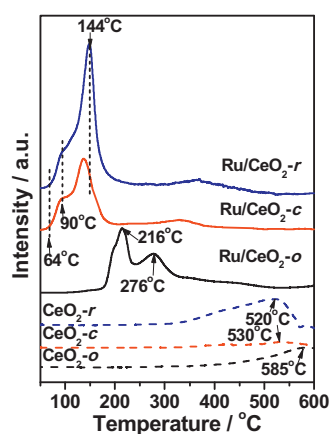
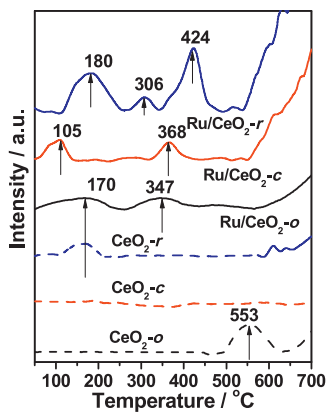


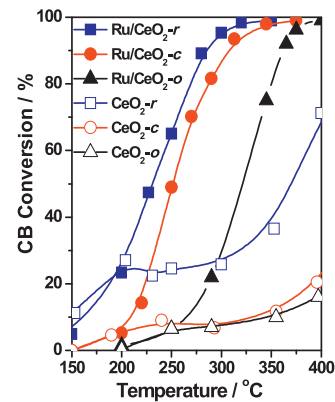
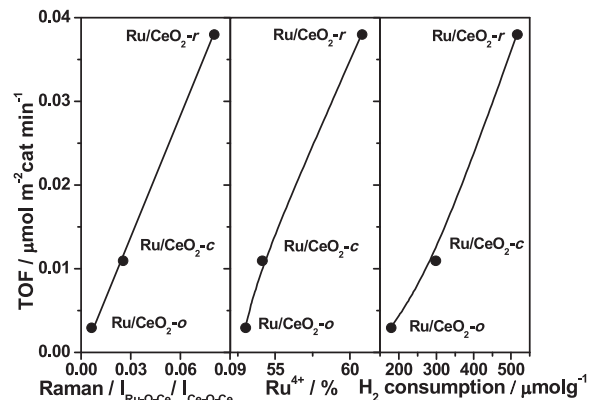
Fig. 7. H<sub>2</sub>-TPR of various CeO<sub>2</sub> and Ru/CeO<sub>2</sub> catalysts.

Fig. 8.  $O_2$ -TPD of various  $CeO_2$  and  $Ru/CeO_2$  catalysts.

the vacancies [60], and the desorption peak appearing at higher temperatures ( $>500^\circ C$ ) can be attributed to the bulk lattice oxygen. Consequently, the amounts of CAOS could be a reflection of the oxygen vacancies from the surface or subsurface of samples [61]. Compared with TPD patterns for  $CeO_2$  samples, the increase in intensity of peaks appearing between 200 and 500  $^\circ C$  for  $Ru/CeO_2$  samples can be observed through the deconvolution of peak areas, indicating that the formation of  $Ru-O-Ce$  can remarkably increase the amount of oxygen vacancies. Moreover, the total amount of chemically adsorbed oxygen species is in the order of  $Ru/CeO_2-r > Ru/CeO_2-c > Ru/CeO_2-o$ , consistent with the results obtained from XRD and Raman (amount of oxygen vacancy in Tables 1 and 2). It can be inferred that CAOS should be related to the interaction between Ru and  $CeO_2$ . Additionally, the original temperature of CAOS desorption follows:  $Ru/CeO_2-r > Ru/CeO_2-c > Ru/CeO_2-o$ , indicating that a much stronger interaction of Ru and  $CeO_2$  exist in  $Ru/CeO_2-r$ , leading to more formation of  $Ru-O-Ce$  bonds. The oxygen molecules from gas phase can adsorb on  $Ru-O-Ce$  under reaction conditions and be activated to form active  $O_2^-$  or  $O^-$  species, which are easily desorbed below 500  $^\circ C$ . According to all results of characterization, it should be expected that  $Ru/CeO_2-r$  with a large amount of  $Ru-O-Ce$  and CAOS possesses excellent catalytic performance for CB oxidative decomposition at low temperature.

#### 3.4. Catalytic activity, stability, $E_a$ and by-products

Fig. 9 shows the catalytic performance of various catalysts for the oxidative decomposition of CB. For pure  $CeO_2$  samples, only  $CeO_2-r$  presents significant activity and CB conversion reaches 68% at 400  $^\circ C$ . While for  $CeO_2-c$  and  $CeO_2-o$  samples, the temperature needed for 20% conversion is 390 and 415  $^\circ C$ , respectively. On the conversion curve, there occurs a plat section within 225–325  $^\circ C$ , which can be ascribed to the deactivation of  $CeO_2$  nanoparticles, due to strong adsorption of Cl species produced during CB decomposition, as reported previously by our group [62,63]. High activity of  $CeO_2-r$  can be ascribed to its high oxygen mobility (Figs. 7 and 8).

Fig. 9. Conversion of chlorobenzene over various  $CeO_2$  and  $Ru/CeO_2$  catalysts. CB concentration: 1000 ppm; GHSV: 30,000  $h^{-1}$ ; catalyst amount: 200 mg.Fig. 10. The effects of contents of  $Ru-O-Ce$  bonds,  $Ru^{4+}$  ions, and oxygen mobility on the activity of  $Ru/CeO_2$  catalysts at 160  $^\circ C$ . CB concentration: 1000 ppm; GHSV: 30,000  $h^{-1}$ ; catalyst amount: 200 mg.

which is critical to removal of Cl species from the surface of catalysts. With the incorporation of Ru into  $CeO_2$  nanoparticles, the conversion curve shifts to lower temperature to a great extent, dependent on the morphological/structural of  $CeO_2$  nanoparticles. For  $Ru/CeO_2-r$  and  $Ru/CeO_2-c$  samples, CB conversion reaches 90% at 283 and 307  $^\circ C$ , much lower than  $Ru/CeO_2-o$  sample over which 90% conversion occurs at 362  $^\circ C$ .  $TOF_{SA}$  at 160  $^\circ C$  is calculated based on the mole of molecules transformed per minute and per the surface area of the catalysts to be 0.038, 0.011 and 0.003  $\mu\text{mol m}^{-2} \text{min}^{-1}$  for  $Ru/CeO_2-r$ ,  $Ru/CeO_2-c$  and  $Ru/CeO_2-o$  samples (Table 4), respectively. As shown in Fig. 10, the plots of the above  $TOF_{SA}$  vis  $Ru-O-Ce$  bond intensity, the content of  $Ru^{4+}$  and  $H_2$  consumption are almost proportional. Considering the other activity parameter for combustion reaction, the temperature needed for 50% conversion of CB ( $T_{50\%}$ ), we compare the above three key properties with  $T_{50\%}$  values and find that the activity in term of  $T_{50\%}$  values are still proportional to the key properties (Fig. S5). These phenomena indicate that the activity for CB oxidation is

**Table 4**

Activity of catalysts and the distribution of Dichlorobenzene and  $Cl_2$ .

Sample	CB oxidation		Chlorinated byproduct			$S_{Cl_2}(\%)$
	$TOF_{SA}^a$ ( $\mu\text{mol m}^{-2} \text{min}^{-1}$ )	$E_a$ (kJ/mol)	Dichlorobenzene (ppm)	$1,3\text{-PhCl}_2$	$1,4\text{-PhCl}_2$	$1,2\text{-PhCl}_2$
$Ru/CeO_2-r$	0.038	49.8	0.6	2.8	0.7	32.5
$Ru/CeO_2-c$	0.011	68.8	1.3	3.3	0	32.5
$Ru/CeO_2-o$	0.003	71.4	2.4	9.0	8.6	25.7

<sup>a</sup> TOF at 160  $^\circ C$  normalized for surface.

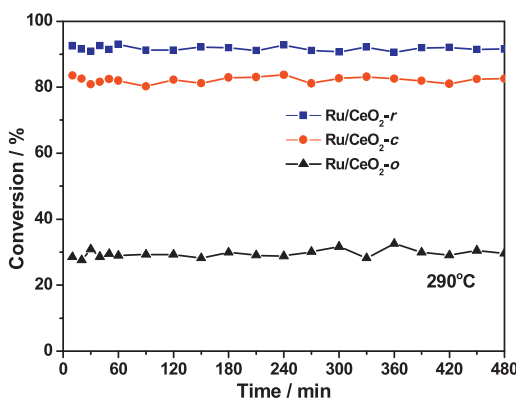


Fig. 11. The stability of chlorobenzene over different Ru/CeO<sub>2</sub> catalysts at 290 °C. CB concentration: 1000 ppm; GHSV: 30,000 h<sup>-1</sup>; catalyst amount: 200 mg.

directly proportional to oxygen mobility, which, in turn, is dependent of the structure of crystal plane of CeO<sub>2</sub>. Clearly, the activity order of Ru/CeO<sub>2</sub> samples is demonstrated as {110} > {100} > {111}. It should be noted that the difference in the activity between Ru/CeO<sub>2</sub>-r and Ru/CeO<sub>2</sub>-c or Ru/CeO<sub>2</sub>-o is noticeably reduced. This phenomenon can be explained that with Ru introduction, the formation of Ru–O–Ce greatly promotes the removal of Cl species, due to the improvement of oxygen mobility (Figs. 7 and 8), especially for CeO<sub>2</sub>-c and CeO<sub>2</sub>-o catalysts, which possess very low oxygen mobility without Ru. However, the formation of Ru–O–Ce is the most on Ru/CeO<sub>2</sub>-r, leading to the highest activity for CB oxidation. Therefore, the activity of either pure CeO<sub>2</sub> supports or Ru/CeO<sub>2</sub> catalysts is dependent of the morphology effect of CeO<sub>2</sub>.

Maintaining the reaction temperature at 290 °C, stable conversions over Ru/CeO<sub>2</sub>-r, Ru/CeO<sub>2</sub>-c and Ru/CeO<sub>2</sub>-o catalysts can be obtained within 8 h, being 92, 82 and 23%, respectively (Fig. 11), indicating that Ru/CeO<sub>2</sub>-r catalyst possesses the highest stable activity. Taking the concentration of O<sub>2</sub> and CB having no significant change within 20% conversion, the temperature dependence of the reaction rate can be used to generate apparent activation energies (Fig. 12). The associated Ea values with 95% confidence limits of CB conversion over Ru/CeO<sub>2</sub>-r, Ru/CeO<sub>2</sub>-c and Ru/CeO<sub>2</sub>-o samples are 49.8, 61.8 and 71.4 kJ mol<sup>-1</sup> within the experimental temperature range (Table 4). It is clear that the activity of Ru/CeO<sub>2</sub>-r is higher than Ru/CeO<sub>2</sub>-c and Ru/CeO<sub>2</sub>-o samples.

The analyses for products in the effluent show that main products are CO<sub>2</sub> (Fig. S6), HCl and Cl<sub>2</sub>. For the products of CB chlorination, dichlorobenzenes (PhCl<sub>2</sub>) are only detected at 250 °C or higher and mainly composed of 1,4-PhCl<sub>2</sub> and 1,2-PhCl<sub>2</sub> with the highest concentration of 3.5, 4.5 and 18 ppm for Ru/CeO<sub>2</sub>-r, Ru/CeO<sub>2</sub>-c and Ru/CeO<sub>2</sub>-o samples, respectively (Fig. 13). The

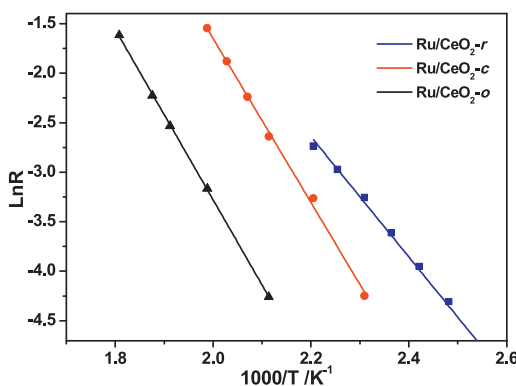


Fig. 12. Arrhenius plots of Ln R versus 1000/T for CB catalytic combustion over different shaped Ru/CeO<sub>2</sub> catalysts.

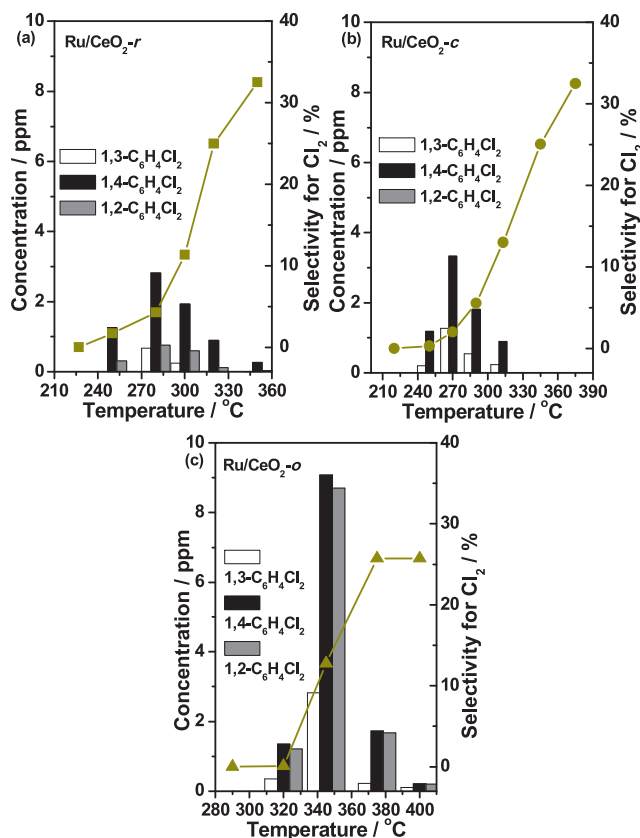


Fig. 13. The selection of Cl<sub>2</sub> and the distribution of dichlorobenzene over Ru/CeO<sub>2</sub>-r (a), Ru/CeO<sub>2</sub>-c (b) and Ru/CeO<sub>2</sub>-o (c) catalysts.

distribution of PhCl<sub>2</sub> and Cl<sub>2</sub> are listed in Table 4. Considering that the activity for PhCl<sub>2</sub> combustion over Ru/CeO<sub>2</sub> catalysts under study is similar to that for CB combustion (not showed), most of PhCl<sub>2</sub> formed during the reaction can be converted, due to the occurrence of chlorination at a significantly high temperature. The amount of PhCl<sub>2</sub> produced is dependent on the activity of Ru/CeO<sub>2</sub> samples for the oxidation of chlorinated benzene. The smaller amount of PhCl<sub>2</sub> over Ru/CeO<sub>2</sub>-r is related to its high activity for the oxidation of CB.

#### 4. Conclusions

In summary, we have first time prepared Ru catalysts supported on ceria nanoparticles with well-defined surface planes by wet impregnation and used them for CB oxidation. It has been revealed that the effect of shape/crystal plane is a key factor which can influence the interactions between Ru species and CeO<sub>2</sub> supports. The CeO<sub>2</sub>-r enclosed by {110} and {100} planes is most favorable for ruthenium stabilization/activation, leading to a larger number of Ru–O–Ce bonds, higher content of Ru<sup>4+</sup> and surface oxygen mobility (H<sub>2</sub> consumption) which results in a lower activation energies (Ea) for CB oxidation. These results will be helpful for understanding the behavior of other previous metal catalysts supported CeO<sub>2</sub> with different shape/crystal plane in the CVOC oxidation and for developing highly active catalyst system.

#### Acknowledgments

We would like to acknowledge the financial support from National Basic Research Program of China (No. 2010CB732300) and National Natural Science Foundation of China (No. 21307033, 21277047) and Shanghai Natural Science Foundation (No.

13ZR1411000), Young Teachers in Shanghai Universities, Commission of Science and Technology of Shanghai Municipality (No. 11JC1402900).

## Appendix A. Supplementary data

Supplementary material related to this article can be found, in the online version, at <http://dx.doi.org/10.1016/j.apcatb.2014.01.062>.

## References

- [1] E. Dobrzyńska, M. Pośniak, M. Szewczyńska, B. Buszewski, *Crit. Rev. Anal. Chem.* 40 (2010) 41–57.
- [2] T. Sakurai, R. Weber, S. Ueno, J. Nishino, M. Tanaka, *Chemosphere* 53 (2003) 619–625.
- [3] G.J. Hutchings, C.S. Heneghan, I.D. Hudson, S.H. Taylor, *Nature* 384 (1996) 341–343.
- [4] R.W. van den Brink, R. Louw, P. Mulder, *Appl. Catal. B Environ.* 16 (1998) 219–226.
- [5] S. Scirè, S. Minicò, C. Crisafulli, *Appl. Catal. B Environ.* 45 (2003) 117–125.
- [6] M. Taralunga, B. Innocent, J. Mijoin, P. Magnoux, *Appl. Catal. B Environ.* 75 (2007) 139–146.
- [7] R. Weber, T. Sakurai, H. Hagenmaier, *Appl. Catal. B Environ.* 20 (1999) 249–256.
- [8] A.M. Padilla, J. Corella, J.M. Toledo, *Appl. Catal. B Environ.* 22 (1999) 107–121.
- [9] Y. Liu, M.F. Luo, Z.B. Wei, Q. Xin, P.L. Ying, C. Li, *Appl. Catal. B Environ.* 29 (2001) 61–67.
- [10] S. Lomnicki, J. Lichtenberger, Z.T. Xu, M. Waters, J. Kosman, M.D. Amiridis, *Appl. Catal. B Environ.* 46 (2003) 105–119.
- [11] F. Bertinchamps, C. Gregoire, E.M. Gaigneaux, *Appl. Catal. B Environ.* 66 (2006) 1–9.
- [12] M. Taralunga, J. Mijoin, P. Magnoux, *Appl. Catal. B Environ.* 60 (2005) 163–171.
- [13] X.Y. Wang, Q. Kang, D. Li, *Catal. Commun.* 9 (2008) 2158–2162.
- [14] X.Y. Wang, Q. Kang, D. Li, *Appl. Catal. B Environ.* 86 (2009) 166–175.
- [15] M. Wu, X.Y. Wang, Q.G. Dai, Kang, D. Li, *Catal. Commun.* 11 (2010) 1022–1025.
- [16] Y. Dai, X.Y. Wang, D. Li, Q.G. Dai, J. Hazard. Mater. 188 (2011) 132–139.
- [17] Y. Dai, X.Y. Wang, Q.G. Dai, D. Li, *Appl. Catal. B Environ.* 111–112 (2012) 141–149.
- [18] M. Baudin, M. Wojcik, K. Hermansson, *Surf. Sci.* 468 (2000) 51–61.
- [19] M. Nolan, S. Grigoleit, D.C. Sayle, S.C. Parker, G.W. Watson, *Surf. Sci.* 576 (2005) 217–229.
- [20] M. Nolan, S.C. Parker, G.W. Watson, *Surf. Sci.* 595 (2005) 223–232.
- [21] M. Nolan, J.E. Fearon, G.W. Watson, *Solid State Ionics* 177 (2006) 3069–3074.
- [22] M. Nolan, G.W. Watson, *J. Phys. Chem. B* 110 (2006) 16600–16606.
- [23] M. Hatanaka, N. Takahashi, T. Tanabe, Y. Nagai, K. Dohmae, Y. Aoki, T. Yoshida, H. Shinjoh, *Appl. Catal. B Environ.* 99 (2010) 336–342.
- [24] M. Nolan, *J. Mater. Chem.* 21 (2011) 9160–9168.
- [25] K.B. Zhou, X. Wang, X.M. Sun, Q. Peng, Y.D. Li, *J. Catal.* 229 (2005) 206–212.
- [26] H.X. Mai, L.D. Sun, Y.W. Zhang, R. Si, W. Feng, H.P. Zhang, H.C. Liu, C.H. Yan, *J. Phys. Chem. B* 109 (2005) 24380–24385.
- [27] L. Yan, R. Yu, J. Chen, X.R. Xing, *Cryst. Growth Des.* 8 (2008) 1474–1477.
- [28] Z.L. Wu, M.J. Li, S.H. Overbury, *J. Catal.* 285 (2012) 61–73.
- [29] Q.G. Dai, H. Huang, Y. Zhu, W. Deng, S.X. Bai, X.Y. Wang, G.Z. Lu, *Appl. Catal. B Environ.* 117–118 (2012) 360–368.
- [30] L.T. Murciano, A. Gilbank, B. Puertolas, T. Garcia, B. Solsona, D. Chadwick, *Appl. Catal. B Environ.* 132–133 (2013) 116–122.
- [31] R. Si, M.F. Stephanopoulos, *Angew. Chem. Int. Ed.* 47 (2008) 2884–2887.
- [32] S.J. Chang, M. Li, Q. Hua, L.J. Zhang, Y.S. Ma, B.J. Ye, W.X. Huang, *J. Catal.* 293 (2012) 195–204.
- [33] L.J. Liu, Z.J. Yao, Y. Deng, F. Gao, B. Liu, L. Dong, *ChemCatChem* 3 (2011) 978–989.
- [34] Q.G. Dai, S.X. Bai, Z.Y. Wang, X.Y. Wang, G.Z. Lu, *Appl. Catal. B Environ.* 126 (2012) 64–75.
- [35] Q.G. Dai, S.X. Bai, X.Y. Wang, G.Z. Lu, *Appl. Catal. B Environ.* 129 (2013) 580–588.
- [36] J.R. González-Velasco, A. Aranzabal, R. López-Fonseca, R. Ferret, J.A. González-Marcos, *Appl. Catal. B Environ.* 24 (2000) 33–43.
- [37] R. López-Fonseca, A. Aranzabal, J.I. Gutiérrez-Ortiz, J.I. Álvarez-Uriarte, J.R. González-Velasco, *Appl. Catal. B Environ.* 30 (2001) 303–313.
- [38] R. Si, Y.W. Zhang, S.J. Li, B.X. Lin, C.H. Yan, *J. Phys. Chem. B* 108 (2004) 12481–12488.
- [39] B. Jägera, A. Stollea, P. Scholza, M. Müllerb, B. Ondruschkaa, *Appl. Catal. A Gen.* 403 (2011) 152–160.
- [40] J. Okal, M. Zawadzki, W. Tylus, *Appl. Catal. B Environ.* 101 (2011) 548–559.
- [41] S. Hosokawa, H. Kanai, K. Utani, Y. Taniguchi, Y. Saito, S. Immamura, *Appl. Catal. B Environ.* 45 (2003) 181–187.
- [42] S.Y. Mar, C.S. Chen, Y.S. Huang, K.K. Tiong, *Appl. Surf. Sci.* 90 (1995) 497–504.
- [43] A. Satsuma, M. Yanagihara, J. Ohyama, K. Shimizu, *Catal. Today* 201 (2013) 62–67.
- [44] H.Y.H. Chan, C.G. Takoudis, M.J. Weaver, *J. Catal.* 172 (1997) 336–345.
- [45] N. Weinstock, H. Schulze, A. Müller, *J. Appl. Phys.* 59 (1973) 5063–5067.
- [46] H.C. Jo, K.M. Kim, H. Cheong, S.H. Lee, S.K. Deb, *Electrochim. Solid. State Lett.* 8 (2005) E39–E41.
- [47] W. Lin, A.A. Herzing, C.J. Kiely, I.E. Wachs, *J. Phys. Chem. C* 112 (2008) 5942–5951.
- [48] Z. Wu, M. Li, J. Howe, H.M. Meyer, *Langmuir* 26 (2010) 16595–16606.
- [49] H.T. Chen, *J. Phys. Chem. C* 116 (2012) 6239–6246.
- [50] A. Bensalem, J.C. Muller, F. Bozon-Verduraz, *J. Chem. Soc. Faraday Trans.* 88 (1992) 153–154.
- [51] N. Kitamura, S. Ishizaka, H.-B. Kim, *Anal. Sci.* 13 (1997) 791–796.
- [52] M. Alam Khan, Do Hung Han, O. Bong Yang, *Appl. Surf. Sci.* 255 (2009) 3687–3690.
- [53] K.S. Kim, N. Winograd, *J. Catal.* 35 (1947) 66–72.
- [54] H.C. Yao, Y.F.Y. Yao, *J. Catal.* 86 (1984) 254–265.
- [55] L. Li, F. Chen, J.-Q. Lu, M.-F. Luo, *J. Phys. Chem. A* 115 (2011) 7972–7977.
- [56] K.-D. Schierbaum, *Surf. Sci.* 399 (1998) 29–38.
- [57] E.S. Putna, J.M. Vohs, R.J. Gorte, *J. Phys. Chem.* 100 (1996) 17862–17865.
- [58] C. Li, K. Domen, K.-I. Maruya, T. Onishi, *J. Am. Chem. Soc.* 111 (1988) 1541–1542.
- [59] P. Li, C. He, J. Cheng, C.Y. Ma, B.J. Dou, Z.P. Hao, *Appl. Catal. B Environ.* 101 (2011) 570–579.
- [60] Z. Zhao, X.G. Yang, Y. Wu, *Appl. Catal. B Environ.* 8 (1996) 281–297.
- [61] C.H. Zhang, C. Wang, W.C. Zhan, Y.L. Guo, Y. Guo, G.Z. Lu, A. Baylet, A.G. Fendler, *Appl. Catal. B Environ.* 129 (2013) 509–516.
- [62] Q.G. Dai, X.Y. Wang, G.Z. Lu, *Catal. Commun.* 8 (2007) 1645–1649.
- [63] Q.G. Dai, X.Y. Wang, G.Z. Lu, *Appl. Catal. B Environ.* 81 (2008) 192–202.